Journal of Materials Chemistry B

ROYAL SOCIETY OF CHEMISTRY

PAPER

View Article Online
View Journal | View Issue

Cite this: J. Mater. Chem. B, 2025, 13, 14032

In vitro and *in vivo* characterization of novel magnesium alloy implants enhanced by hydrothermal and sol–gel treatments for bone regeneration

Daniele Bellavia, †[a] Francesco Paduano, †[b] Silvia Brogini, *[a] Roberta Ruggiero,[b] Rosa Maria Marano,[b] Angela Cusanno,[c] Pasquale Guglielmi,[c] Antonio Piccininni,[c] Matteo Pavarini,[d] Agnese D'Agostino,[e] Alessandro Gambardella,[a] Chiara Peres,[fg] Gianfranco Palumbo,[c] Roberto Chiesa,[d] Gianluca Zappini,[h] Marco Tatullo‡[bi] and Gianluca Giavaresi‡[a]

Magnesium alloys are emerging as promising materials for biodegradable orthopedic implants due to their mechanical strength and biocompatibility. However, their clinical use is hindered by rapid degradation and hydrogen gas evolution, which can compromise implant stability and bone healing. This study investigates the biocompatibility, genotoxicity, and osteointegration of magnesium implants (AZ31) produced *via* Superplastic Forming and enhanced through Hydrothermal and Sol–Gel surface treatments. Both techniques produced uniform $Mg(OH)_2$-based coatings, but only alloy with hydrothermal treatment exhibited a markedly slower *in vitro* degradation. Cytotoxicity and Ames mutagenicity assays confirmed the biocompatibility and non-mutagenic nature of all implant types. *In vivo* evaluation in a rat femoral defect model revealed successful bone formation around all implant types, with comparable trabecular bone area. However, surface-treated implants showed a significantly lower bone-to-implant contact compared to the control AZ31 alloy, with solgel-treated alloys exhibiting an accelerated degradation rate and higher hydrogen release, which may influence tissue integration. These results highlight the role of surface modification in tuning degradation behavior and bone interface characteristics, with solgel-treated alloys resorbing faster. The combination of superplastic forming processing with strategic surface treatments offers a promising approach to achieving controlled biodegradation, although further optimization is needed to improve bone-implant integration. This work supports the further development of surface-engineered Mg implants for safe and functional orthopedic applications.

Received 28th May 2025,
Accepted 19th August 2025

DOI: 10.1039/d5tb01282a

rsc.li/materials-b

1. Introduction

Biodegradable magnesium (Mg)-based metal implants have been demonstrated to promote bone formation, and are particularly appreciated for their mechanical resilience and ability to degrade *in situ*, representing a paradigm shift in bone biomaterials.[1] Indeed, the use of Mg alloys allows the utilization of temporary implants for the fixation of fractured bone, without the need for further surgical interventions that are often required to remove the corresponding permanent fixation systems, thereby reducing patient morbidity and healthcare costs.[2] Furthermore, the Mg released by degradation appears to stimulate osteoblastic differentiation and inhibit osteoclastic differentiation, limiting degradation and promoting the synthesis of new bone, as indicated by various studies, highlighting its dual therapeutic mechanism.[3] However, despite these

[a] SC Scienze e Tecnologie Chirurgiche, IRCCS Istituto Ortopedico Rizzoli, Bologna, 40136, Italy. E-mail: silvia.brogini@ior.it
[b] Stem Cells and Medical Genetics Units, Biomedical Section, Tecnologica Research Institute and Marrelli Health, 88900, Crotone, Italy
[c] Dipartimento di Meccanica, Matematica e Management, Politecnico di Bari, Bari, 70125, Italy
[d] Department of Chemistry, Materials and Chemical Engineering 'G. Natta', Politecnico di Milano, Milan, 20131, Italy
[e] Department of Engineering and Applied Sciences, University of Bergamo, Viale Marconi 5, Dalmine (BG), 24044, Italy
[f] Unit of bologna, CNR-National Research Council of Italy, Institute of Molecular Genetics "Luigi Luca Cavalli-Sforza", 40136 Bologna, Italy
[g] IRCCS Istituto Ortopedico Rizzoli, 40136, Bologna, Italy
[h] Lincotek Medical, Pergine Valsugana, Trento, 38057, Italy
[i] Department of Translational Biomedicine and Neuroscience- DiBraiN, School of Medicine, University of Bari "Aldo Moro", Bari, 70124, Italy
† Co-first authors.
‡ Co-last author.

promising features, Mg implants are currently not widely used for osteosynthesis, for several reasons, including the fact that an initial uncontrolled degradation reaction is often observed, which often results in unfavourable osteosynthesis in patients.[4] More specifically, this fundamental challenge originates from the accelerated degradation kinetics, which generates both significant pH perturbations and hydrogen evolution, ultimately compromising the structural integrity of the implant. Moreover, it leads to the establishment of a strong inflammatory state that affects both the neo-synthesis of bone, the maturation of osteoclasts, and osteolysis.[5] To overcome these limitations, many studies tried to limit this strong initial degradation through the use of novel Mg alloys, and surface modifications, such as through surface oxidation of the devices or implementing specific coatings that can enhance the device's resistance to degradation.[1] Central to this optimization process, the complexity of controlling the relationship between crucial factors such as the processing parameters, the chemical composition, or the mechanical and biological properties, plays a crucial role in developing biomedical devices.

Building upon this foundational understanding, in the pursuit of advanced manufacturing solutions, Superplastic Forming (SPF) has emerged as a particularly promising approach, offering unprecedented control over microstructural evolution during Mg alloy processing while enabling the fabrication of complex, customized geometries.[6–8] During SPF, a metal blank is deformed by the combined effect of elevated temperature (greater than half of the melting temperature), low strain rates, and pressurised gas, which forces the blank to copy the geometry of the die. In this way, customized parts even characterized by complex shapes can be produced with a high shape accuracy.[7] Supporting this innovative approach, the feasibility and effectiveness of SPF in biomedical applications have been recently demonstrated in our comprehensive study comparing SPF and Single Point Incremental Forming (SPIF) techniques for manufacturing titanium cranial prostheses.[9] Significantly, the *in vivo* validation in an ovine model demonstrated that SPF-manufactured prostheses effectively supported bone regeneration while maintaining structural integrity. These findings establish SPF as a promising manufacturing technique for complex medical implants where precise geometrical accuracy is an essential requirement.[9] Recently, this group has demonstrated that Mg alloys (AZ31) manufactured through SPF (Mg_SPF) retain significant osteoinductive and antibacterial properties.[10,11] Specifically, the behavior of these Mg-based devices manufactured *via* the SPF process and functionalized with different coatings was evaluated in different *in vitro* experiments. These included cytotoxicity assessments in both direct and indirect contact, gene expression analyses to assess the differentiation of mesenchymal stem cells into osteoblasts, and antibacterial activity tests, demonstrating their potential to prevent implant-related infections and promote osteogenesis. In particular, Mg_SPF devices promote cellular adhesion while inducing the expression of osteogenesis-related genes such as BMP2 and RUNX-2. Furthermore, these materials have demonstrated significant antimicrobial activity against relevant pathogenic strains, suggesting potential applications in infection-resistant implants.[10,11]

In this study, the biological performance of AZ31 Mg alloy devices manufactured through the SPF process and subsequently modified *via* Hydrothermal and Sol–Gel treatments was investigated. We hypothesized that the combination of SPF with these surface modification techniques could enhance the biocompatibility and osteointegration ability of Mg-based implants. To address the limitations of Mg alloys in biomedical applications, a framework was developed to study the effects of surface treatments on biocompatibility, genotoxicity, and *in vivo* osteointegration. As part of this approach, a preliminary characterization of the modified surfaces was performed to assess their structural, chemical, and functional properties, to elucidate their possible role in biological response modulation. This strategy combined *in vitro* assessments of cellular responses and genotoxicity with *in vivo* studies of tissue-material interactions and bone integration patterns. The approach aimed to evaluate the safety and osteointegration of modified implants, with a focus on the bone–implant interface. This investigation provides insights into how surface modification influences biological responses, offering new perspectives on Mg implants in biomedical applications where controlled tissue integration is crucial.

2. Results and discussion

2.1. Characterization of coatings

This study investigated the biological performance of Mg implants (AZ31) manufactured *via* Superplastic Forming (Mg_SPF) and subsequently modified through hydrothermal (HT_Mg_SPF) and Sol–gel (Solgel_Mg_SPF) surface treatments. The surface morphology of the coated Mg_SPF samples is reported in Fig. 1A, highlighting how the application of the solgel coating results in a smooth, continuous appearance with no noticeable cracks (Solgel_Mg_SPF, left image), while the hydrothermal treatment leads to a regular acicular structure (HT_Mg_SPF, right image). Both surface types show an overall homogeneous structure, although small defects resulting from the coating process are present in the form of micrometric build-ups and clusters, as well as needle-like areas of different sizing in the case of hydrothermal coatings. Nevertheless, both techniques achieve complete surface coverage.

The surface modification of Mg alloys is crucial for improving their degradation behavior. It is generally accepted that rapid degradation is the primary critical issue with Mg alloys, leading to hydrogen production in *peri*-implant tissues, which hinders bone regeneration and limits the osseointegration process. Previous studies have proposed various alloy modifications to improve uniform and controlled degradation rates.[12–14] Among these, inorganic or organic coatings have proven effective in regulating degradation by enhancing the corrosion resistance of the material.[15] Also surface modification strategies or coating techniques such as hydrothermal treatments or sol–gel processes can be aimed at enhancing corrosion resistance and thus controlling the degradation of the material.[16] Our results support these findings, as both coating techniques resulted in

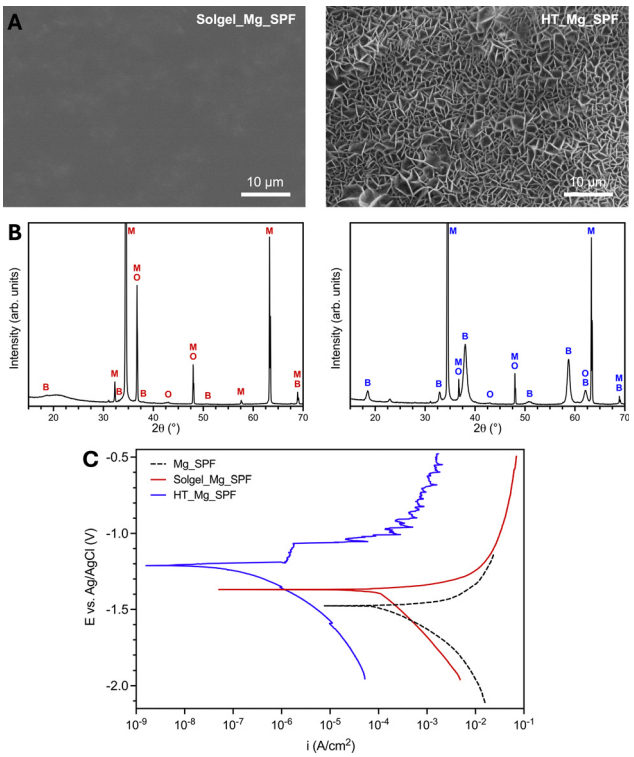

Fig. 1 Morphological, chemical, and functional characterization of Solgel_Mg_SPF and HT_Mg_SPF surfaces. (A) SEM images of the coated samples' surfaces. (B) X-ray diffractograms of the coatings, elucidating their chemical structure. M = magnesium (Mg, ICSD 98-016-8829 and 98-018-1728); O = magnesium oxide (MgO, ICSD 01-075-1525 and 98-024-8386); B = brucite ($Mg(OH)_2$, ICSD 98-008-9823 and 98-024-8985). (C) Representative potentiodynamic polarization curves of the samples compared to the uncoated control (Mg_SPF).

coating that maintained high homogeneity and continuity, which is promising for slowing down corrosion reactions and limiting hydrogen evolution during the initial stages of the degradation process.

In terms of chemical structure, the XRD spectra of both coatings (Fig. 1B) show a predominant Mg phase, mostly ascribable to the underlying substrate contribution given the relatively low thickness of the coatings (<1 μm) and the penetration depth of the technique in such materials. Notably, the Solgel_Mg_SPF coating (left image) featured mixed magnesium oxide and hydroxide peaks, while HT_Mg_SPF coating (right image) appears to be mostly composed of crystalline magnesium hydroxide (brucite) as a result of the conversion process performed in an aqueous environment. These chemical compositions were specifically chosen to ensure that the coatings were ultimately degradable, while also potentially being well-tolerated by the body as they fulfill their protective role. Looking at the degradation behavior of the coatings, the potentiodynamic polarization curves obtained from electrochemical corrosion tests (Fig. 1C) indicate a significant ennoblement of both Solgel_Mg_SPF and HT_Mg_SPF surfaces compared to uncoated Mg_SPF, with a free corrosion potential (E_{corr}) shift toward more positive values for the two coatings (-1.20 ± 0.01 V and -1.35 ± 0.02 V, respectively, *vs.* -1.48 ± 0.03 V of Mg_SPF). Moreover, although the corrosion current density (i_{corr}) of the devices shows no significant differences with the introduction of the solgel coating (181 ± 64 μA cm^{-2} and 135 ± 41 μA cm^{-2} for Mg_SPF and Solgel_Mg_SPF, respectively), it markedly drops when the hydrothermal process is applied (down to 0.03 ± 0.02 μA cm^{-2}), indicating a greater barrier action of the latter against the corrosive medium. Overall, these data suggest a marked protective action of HT_Mg_SPF surfaces, being the most effective in slowing down the degradative process of magnesium in physiological-like conditions, while the solgel coating's effect remains uncertain. The ICP-OES analysis revealed that the average copper content in the Solgel_Mg_SPF coatings was 0.012 ± 0.001 wt%. This relatively low incorporation of copper is consistent with its intended function as a functional dopant, specifically designed to endow the sol–gel matrix with bioactive properties, without compromising its structural integrity. Trace amounts of copper in the range of 0.01–0.1 wt% have been widely reported as effective in achieving antimicrobial activity through the release of Cu^{2+} ions, which generate reactive oxygen species (ROS), disrupt bacterial cell membranes, and inhibit microbial replication.[17] In addition to its antimicrobial function, copper also plays a pivotal role in stimulating bone regeneration. As a trace element essential for skeletal development, copper contributes to angiogenesis and osteogenesis by upregulating vascular endothelial growth factor (VEGF) and promoting osteoblastic differentiation.[18] The Cu^{2+} ions released from the coating interact with surrounding tissues to support new bone formation, matrix mineralization, and vascular infiltration, key processes in effective bone repair. For example, Liu *et al.* demonstrated that magnesium–copper alloys release biologically active Cu^{2+} at concentrations that significantly enhance both osteogenic and angiogenic responses *in vitro*, while simultaneously maintaining long-term antibacterial performance.[19] Therefore, the measured copper content (~0.012 wt%) in Solgel_Mg_SPF coatings appears to be an optimal compromise sufficient to confer dual-function bioactivity (antibacterial and osteoinductive), yet low enough to avoid cytotoxic effects or structural degradation of the sol–gel network. These findings highlight the strategic use of copper as a multifunctional dopant in advanced biomaterial design.

2.2. Cytotoxic activity of Mg-SPF implants

Fig. 2A shows the viability of murine fibroblast L-929 cells, expressed as a percentage relative to cells cultured in extraction mediums derived from Mg_SPF, Solgel_Mg_SPF, and HT_Mg_SPF devices, compared to the negative control over 1, 3, and 7-day periods. The red line at 75% cellular viability demarcates the threshold between cytotoxic materials (below the line) and non-cytotoxic materials (above the line). Mg_SPF were cytotoxic at day 1 (19.65 ± 5.4%) and day 3 (69.2 ± 6.6%) but not at day 7 (91.37 ± 7%). Conversely, extracts from Solgel_Mg_SPF and HT_Mg_SPF devices exhibit no cytotoxicity towards L-929 cells throughout the entire duration. Consequently, Solgel_Mg_SPF and HT_Mg_SPF devices demonstrate highly significant cytocompatibility. Fluorescence-based viability assessment demonstrated differential cellular responses across the Mg substrate variants. Time-course

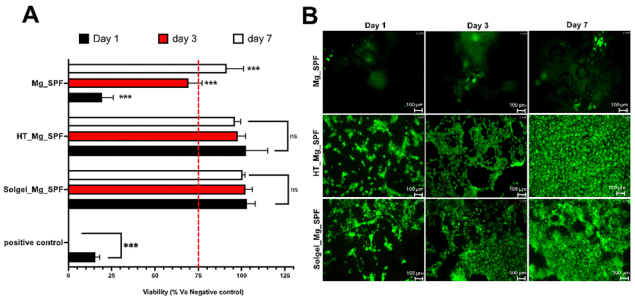

Fig. 2 Indirect cytotoxicity and live/dead assay of Mg_SPF, Solgel_Mg_SPF, and HT_Mg_SPF Implants. (A) Proliferation of L929 cells (% of control) in extract media from Solgel_Mg_SPF and HT_Mg_SPF over 1, 3, and 7 days. 10% dimethyl sulfoxide (DMSO) was used as a positive control, whereas culture medium was used as a negative control. Cell viability values are expressed as percentages normalized to the negative control, set at 100% for each time point. Statistical significance is indicated by ***, $p < 0.001$ compared to the negative control. (B) Representative Live/dead assays of DPSCs seeded on Mg_SPF, Solgel_Mg_SPF, and HT_Mg_SPF implants after 1, 3, and 7 days; green represents live cells; scale bar: 100 μm.

analysis revealed that Solgel_Mg_SPF and HT_Mg_SPF surfaces supported progressive Dental pulp stem cell colonization from day 1 to day 7 (Fig. 2B), with cells exhibiting spindle morphology (see SI)

These modified Mg alloy implants facilitated both initial cell attachment and subsequent population expansion, suggesting optimization of the cell–substrate interface. The temporal increase in viable cell density indicates sustained biocompatibility of the modified surfaces throughout the experimental period. Notably, assessment of cellular behavior on unmodified Mg_SPF was precluded by extensive hydrogen gas evolution, a characteristic consequence of rapid magnesium degradation kinetics. The cumulative evidence from both direct contact studies and extract-based cytotoxicity analyses establishes that hydrothermal and sol–gel modifications effectively enhance the biological properties of magnesium substrates, supporting their potential therapeutic use. *In vitro* analyses demonstrated significant enhancement of implant biocompatibility following surface modifications of Mg alloys, attributed to the formation of stratified protective interface layers that effectively modulated degradation kinetics, acting as a physical barrier against the penetration of degradative media towards the substrate, and facilitated cellular attachment. This enhanced biocompatibility was evidenced by sustained cellular viability and characteristic spindle morphology of dental pulp stem cells cultured on the surface-treated Mg_SPF alloys, with both hydrothermal and sol–gel treatments demonstrating superior cell–material interactions partly thanks to the higher cytocompatibility and stability of magnesium oxide and hydroxide species. In contrast, untreated Mg Alloys (Mg_SPF) exhibited extensive hydrogen evolution and accelerated degradation, which inhibited cellular adhesion and proliferation. This accelerated degradation phenomenon, previously documented by Castro and Durán, represents a fundamental challenge in Mg alloy applications, arising from the inherently high reactivity of these materials in physiological environments.[20] Recent investigations have indeed demonstrated that strategic implementation of Mg alloys with sol–gel and hydrothermal surface modifications, similar to those optimized in the present study, establishes effective barriers between the Mg substrate and physiological medium, thereby modulating degradation kinetics to more favorable rates for biological applications.[21,22]

2.3. Genotoxicity of Mg-SPF implants

The Ames assay was performed to evaluate the genotoxicity of substances released from the surface of the studied implants after the incubation period. The extracts from Mg_SPF, Solgel_Mg_SPF, and HT_Mg_SPF implant alloys did not exhibit mutagenic effects in *Salmonella typhimurium* strains TA1535 and TA1537 at any of the tested concentrations (100%, 75%, 50%, 25%, 12.5%, and 6.25%) either with or without metabolic activation (Fig. 3 and 4). The results indicated no concentration-dependent increase in the mean number of revertant wells. Additionally, none of the extracts produced multiple positive responses with a fold increase (FI) in revertant numbers over the baseline ≥ 2. The positive and negative control values, as well as baseline values, were within acceptable limits, ensuring the validity of the experiment. Therefore, based on the Ames MPF™ Test results, none of the Mg alloy implants (Mg_SPF, Solgel_Mg_SPF, and HT_Mg_SPF) demonstrated mutagenic properties (Fig. 3 and 4). Such a comprehensive genotoxicity assessment demonstrated the absence of mutagenic potential across all SPF-manufactured Mg alloy

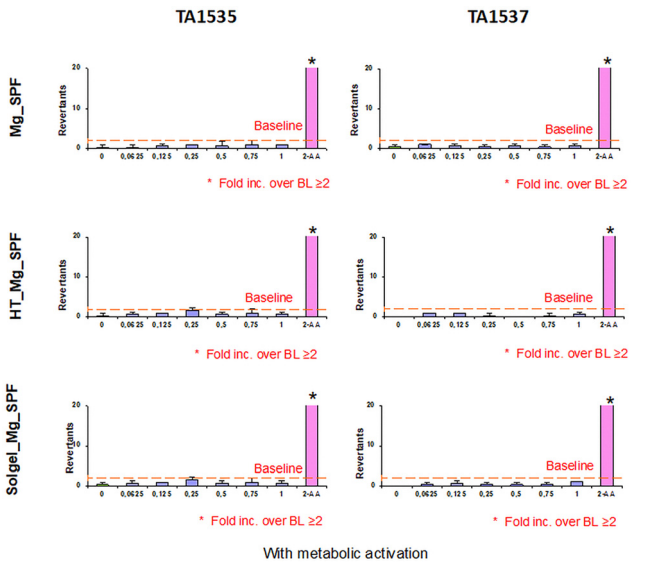

Fig. 3 Ames test of Mg_SPF, HT_Mg_SPF, and Solgel_Mg_SPF implants without metabolic activation. The negative control utilized cell culture medium (0), while positive controls included N4-aminocytidine (N4-ACT) for TA1535 and 9-aminoacridine (9-AAC) for TA1537 without S9 (metabolic activation). The number of revertant bacterial colonies corresponds to the mutagenic potential of the analyzed Mg implants. None of the Mg implants demonstrated genotoxic potential in any of the bacteria strains in this assay. 0.0625, 0.125, 0.25, 0.5, 0.75, and 1 correspond to the tested concentrations of 6.25%, 12.5%, 25%, 50%, 75%, and 100%, respectively. BL; baseline.

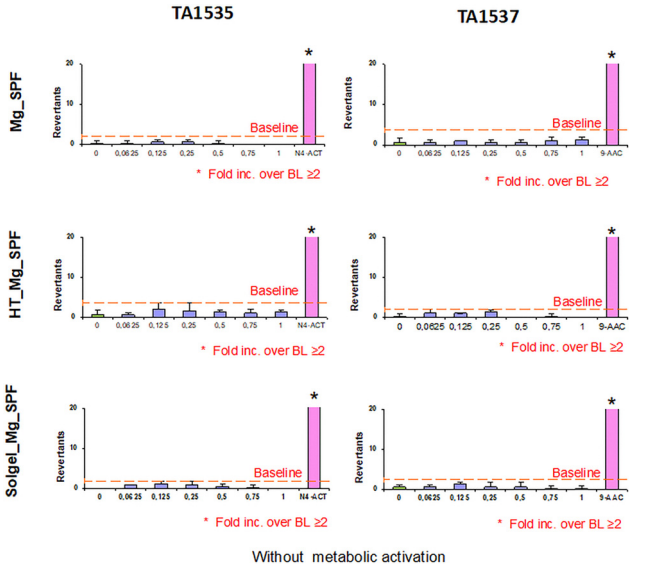

Fig. 4 Ames test of Mg_SPF, HT_Mg_SPF, and Solgel_Mg_SPF implants with metabolic activation. The negative control utilized cell culture medium (0), while positive controls included 2-aminoanthracene (2-AA) for both TA1535 and TA1537 with S9 (metabolic activation). The number of revertant bacterial colonies corresponds to the mutagenic potential of the analyzed Mg implants. None of the Mg implants demonstrated genotoxic potential in any of the bacteria strains in this assay. 0.0625, 0.125, 0.25, 0.5, 0.75, and 1 correspond to the tested concentrations of 6.25%, 12.5%, 25%, 50%, 75%, and 100%, respectively. BL; baseline.

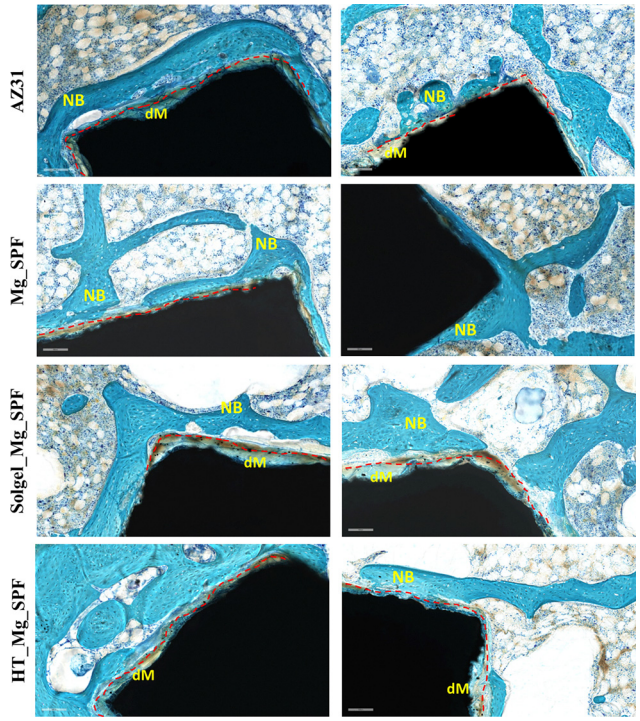

Fig. 5 Representative histological images of AZ31 magnesium alloy implants. Magnification, 20×; scale bar 100 μm; dM = degraded material; NB = new bone; staining: Stevenel's blue and fast green.

variants, both surface-treated and untreated, corroborating previous findings on similar Mg-based devices.[23,24] This non-mutagenic profile, combined with the enhanced biocompatibility of the surface-modified SPF Mg alloys, provides compelling evidence supporting the potential clinical translation of these SPF-manufactured Mg alloys as biodegradable implant materials.

2.4. *In vivo* study

All animals successfully reached the experimental endpoint without any adverse events, allowing for the inclusion of all subjects in the analysis. Throughout the experimental period, the animals were monitored weekly, with particular attention given to changes in body weight. The average weekly weight gain was 9.98 ± 0.43 g, suggesting no negative health effects from the healing process, implant degradation, or osteointegration. No signs of inflammation or necrosis were observed in the *peri*-implant tissues, and in most cases, the implant site was still visible with partial regeneration of the epiphyseal cortex.

2.4.1. Histology and histomorphometry. Histological analysis showed that all implants were well integrated with the surrounding bone tissue. The epiphyseal trabecular architecture appeared normal, with no inflammatory, necrotic, or fibrous reactions around the implants. Stevenel's Blue staining highlighted that the new bone, distinguished by its darker blue colour and rounder osteocyte lacunae compared to the pre-existing bone, consisted of trabeculae with varying degrees of lamellar organization according to maturation level, resembling mature trabecular bone (Fig. 5).

Upon closer examination, the newly formed bone was found to be in direct contact with most of the AZ31 and Mg-SPF implant perimeters, seamlessly merging with the surrounding native bone (Fig. 5). In contrast, a thin layer of immature bone-like matrix was detected between the implant and *peri*-implant bone around the Solgel_Mg_SPF (Fig. 6A) and HT_Mg_SPF (Fig. 6B) perimeters, reducing the contact surface.

At higher magnification, this tissue appeared to be a bone matrix in an early developmental stage, distinctly separated from the implant border by medullary cavities containing identifiable cells (Fig. 7). Most of the contact between the bone and material occurred at the implant's corners.

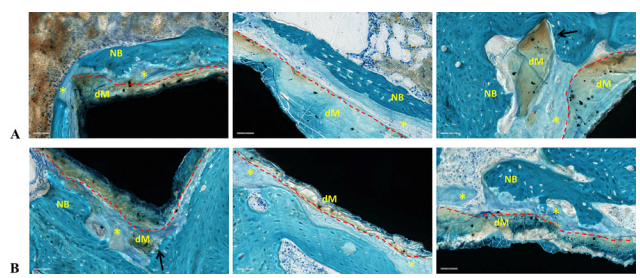

Fig. 6 Representative images of Solgel_Mg_SPF (A) and HT_Mg_SPF (B) implants. The presence of an amorphous bone-like matrix between the implant perimeter (dotted red line) and the new bone (NB) is indicated by the asterisk (*); degradation of the material is also evidenced by the dotted red line (dM = degraded material). The black arrows highlight areas of the implant that appear broken. Magnification, 40×; scale bar 50 μm; staining: Stevenel's blue and fast green.

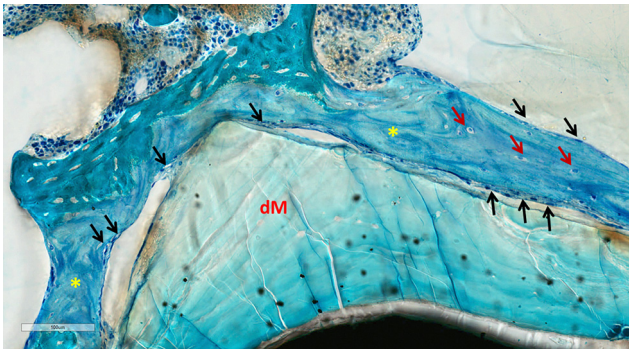

Fig. 7 Representative histological image showing the immature bone-like matrix (yellow asterix) at the implant interface. Embedded cells (future osteocytes; red arrows) are visible within the matrix, and continuous cellular layers (osteoblasts; black arrows) are observed along the margins; dM= degraded material; magnification 20×; scale bar: 100 μm.

Additionally, the degradation of the Mg implants was evident from the irregular shape of the implant perimeters and the shadow of the original implant (Fig. 5 and 6; indicated by dotted red lines). Some parts of the degraded implants appeared broken (Fig. 6, black arrows), which could be attributed to the concurrent material degradation and bone growth processes that may have contributed to the detachment of small debris.

Additionally, the formation of gas bubbles (Fig. 8)—a hallmark of Mg degradation—was observed in the Solgel_Mg_SPF implants, characterized by the circular growth of the surrounding new bone (Fig. 8C).

Regarding histomorphometric analysis, the native epiphyseal trabecular bone showed the following values (n = 24): trabecular bone area (B.Ar/T.Ar) was 40 ± 8%, trabecular thickness (Tb.Th) was 0.25 ± 0.06 mm, trabecular number (Tb.N) was 1.70 ± 0.51 mm, and trabecular bone separation

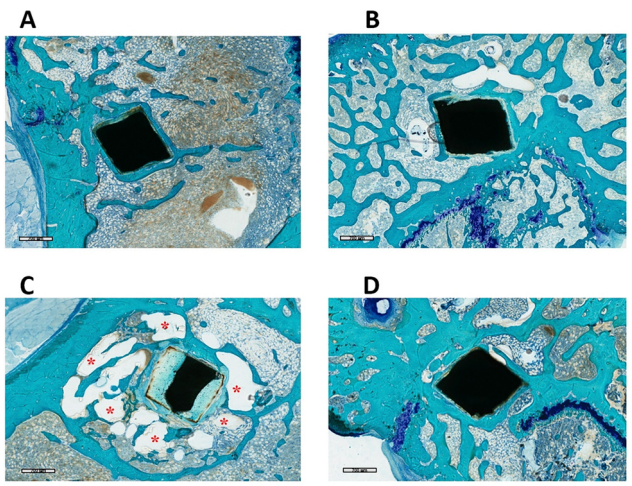

Fig. 8 Representative images of _Mg implants. (A) AZ31; (B) Mg_SPF; (C) Solgel_Mg_SPF; (D) HT_Mg_SPF. The presence of gas bubbles is visible around the Solgel_Mg_SPF implant (C, red *) as well as a circular growth pattern of the surrounding bone tissue. Magnification, 3×; scale bar 700 μm; Staining: Stevenel's Blue and Fast Green.

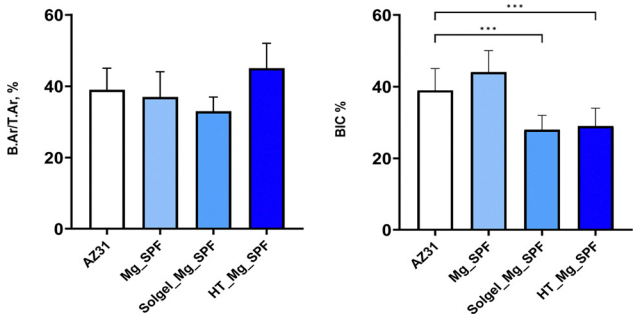

Fig. 9 B.Ar/T.Ar, % and BIC, % results. Histograms on the results of *peri*-implant trabecular bone tissue (B.Ar/T.Ar, %) and bone surface contact (BIC, %) present around the Mg alloy devices. Mean ± SD, n = 12. Dunnett test *versus* control (AZ31): ***, $p < 0.001$.

(Tb.Sp) was 0.10 ± 0.03 mm. Fig. 9 presents the B.Ar/T.Ar and BIC results. Statistical analysis revealed no significant differences in the B.Ar/T.Ar parameter across implant types, showing values very similar to those of healthy trabecular epiphyseal bone. However, a significant reduction in the BIC values (F = 24.1, $p < 0.001$) was observed for the Solgel_Mg_SPF and HT_Mg_SPF implants compared to the control AZ31, at 28% and 25%, respectively.

The BIC results suggest that both Solgel_Mg_SPF and HT_Mg_SPF alloys obtained similar osseointegration, lower than that of AZ31 implants, for the healing time investigated. It is important to be cautious when comparing BIC among different studies, as there is considerable variability among experiments. This includes factors such as the shape of the implant, the implantation site, or the thickness of the histological sections. The observed values are likely attributable to the presence of the thin biomimicking bone-like matrix separating the material from the newly formed bone that resembles immature trabecular bone. Unfortunately, the limited experimental time did not allow for an investigation into whether this tissue could eventually be replaced by more mineralized bone tissue. Current histological observations of this tissue are similar to those reported by Lee *et al.*[25] They observed that conventional histological methods (Von Kossa, toluidine blue, and Goldner's trichrome staining) do not reveal an acellular matrix, whereas Villanueva staining and fluorescence microscopy highlight the reactive Mg alloy interface. Lee *et al.* identified three regions at the Mg alloy–implant interface: region I, with an amorphous structure rich in magnesium and oxygen; region II and region II', which differ because region II' has a crystalline structure, specifically a calcium phosphate phase, suggesting a more complex process than in regions I and II; and region III, which has a bone-like microstructure. Given the findings of Lee *et al.*, it is plausible that the tissue observed in this work corresponds to regions II′–III, where a crystallization process of calcium- and phosphorus-rich compounds occurs prior to the formation of mature bone tissue. Furthermore, the production of gas bubbles, especially in the Solgel_Mg_SPF implants, may interfere with the direct apposition of newly formed bone.

Gas formation during the degradation of Mg and its alloys is one of the main issues limiting the use of these materials,

especially in the biomedical field. The hydrogen produced does not readily dissolve in the tissue, resulting in the formation of gas bubbles around the material, which may accumulate in a localised manner. The formation of gas bubbles can result in elevated localised pressure, which may impede the normal healing process of the tissue.[26] This can lead to several complications, including inflammation, alterations in bone microstructure, the formation of cavities in surrounding tissues, and, at worst, a decrease in the animal survival rate.[14] Nevertheless, all animals reached the experimental endpoint, and the histological analysis did not reveal obvious adverse tissue reactions around the alloys. Subsequently, upon the onset of degradation, a state of simultaneous bone resorption and formation was observed. Chang *et al.* evaluated bone microstructural, histomorphometric, and biomechanical properties of high-purity Mg screws (HP-Mg) in epiphyseal trabecular bone of rabbits at various time points (4, 8, and 16 weeks).[27] They observed the formation of cavities/bubbles without bone growth at all three time points, even though they stated that their amount and size appeared to decrease at 8- and 16-week post-implantation. Furthermore, similar to our findings, an amorphous matrix layer was also observed accompanied by Mg degradation. Thus, according to our results, Mg implants appeared to enhance *peri*-implant bone remodelling accompanied by the formation of *peri*-implant cavities.

Additionally, a significant increase in the implant degradation area (IDAr) for Solgel_Mg_SPF implants (38.8%; $F = 185$, $p < 0.001$) was noted, along with a variation in implant surface area (dISAr) parameters (137%; $F = 165$, $p < 0.001$) (Fig. 10) compared to the control material. The above *in vivo* results showed a significantly higher degradation of Solgel_Mg_SPF implants with respect to the AZ31 control and the other types of implants. The observed trend aligns with the electrochemical corrosion tests, as well as with the expectedly low thickness of the applied solgel coatings (<1 μm), suggesting a potentially higher performance of the hydrothermal treatment in preventing corrosion. Interestingly, 38.8% of the initial volume of Solgel_Mg_SPF implants was degraded after 12 weeks of implantation. This value is close to that of 34% highlighted by Lee *et al.*, although at 16 weeks.[25] Such a tendency of Solgel_Mg_SPF implants may be due to different causes. Firstly, the degradation of Mg, which is common to all materials tested, typically increases the pH, creating a more basic environment in the surrounding tissues. The corrosion reaction of magnesium results in the formation of hydroxyl ions, which raise the pH. Nevertheless, an elevated pH level tends to impede the degradation of magnesium even further as the environment becomes less conducive to the continued degradation of the material. The medullary cavities, being highly vascularized, have a superior ability to remove magnesium degradation products, thus neutralizing the pH increase more rapidly through blood buffering and the removal of degradation byproducts. This buffering capacity helps maintain a more neutral pH, which prevents the corrosion from being slowed down as much as it would be in other areas with less vascularization. Consequently, the degradation of magnesium in the bone marrow can occur at a faster rate than in other areas.[28] Therefore, the degradation process is faster in the bone marrow than in areas with less vascularization or pH-neutralizing capacity.[29] However, the accelerated degradation observed in Solgel_Mg_SPF implants is likely due to the unique combination of copper ion incorporation in the sol–gel treatment and the implantation site in highly vascularized areas. Copper ions, which are present only in the sol–gel treated samples, are known to promote localized electrochemical reactions, further accelerating the corrosion process. As a result, while the basic mechanism of magnesium corrosion is common across all materials tested, the presence of copper in the Solgel_Mg_SPF implants leads to faster degradation rates in these specific conditions, particularly in highly vascularized environments.

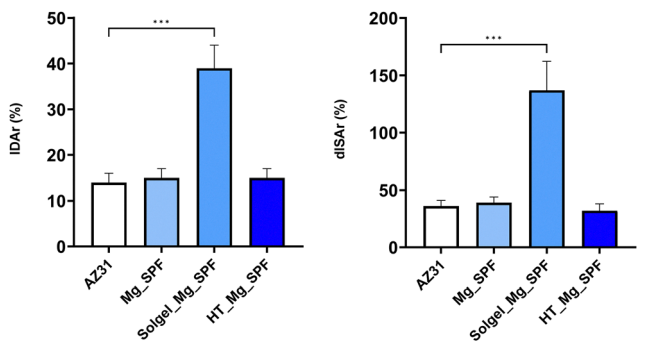

Fig. 10 IDAr, % and dISAr, % results. Histograms on the results of implant degradation area (IDAr, %) and implant surface area variation (dISAr, %). Mean ± SD, $n = 12$. Dunnett test *versus* control (AZ31): ***, $p < 0.001$.

Several studies have shown that elements such as Cu can increase intergranular corrosion (IGC) in some metal alloys, altering the chemical stability of the coating and reducing its protective effectiveness over time. Furthermore, in humid or corrosive environments, Cu ions can migrate through the coating and interact with magnesium, worsening corrosion resistance and promoting localized corrosion phenomena. The presence of Cu can alter the electrochemical potential of the surface, making the underlying Mg more susceptible to corrosive attack.[30–32] From the material perspective, Cu alloying tends to accelerate magnesium degradation and reduce its mechanical properties. However, it is important to note that in our Solgel_Mg_SPF implants, Cu was present exclusively in the surface coating and not alloyed with the magnesium substrate. EDS analyses (Fig. 10) performed confirmed the absence of Cu in the residual material. Therefore, we hypothesize that the higher degradation observed in the Solgel_Mg_SPF group is due to the combined effect of both the implantation site and the surface treatment. While the Cu in the surface coating may have a role in the early post-implantation phase, the more pronounced degradation in the Solgel_Mg_SPF implants is likely driven by the overall effect of both factors working together. However, in orthopaedic applications such as the repair of bone defects or the treatment of osteomyelitis, the natural degradation of these materials may prove advantageous.

Furthermore, it is possible to regulate the rate of degradation by modulating the copper content to meet clinical needs.

Consequently, Mg–Cu alloys may offer a suitable solution. Even though there has been very little research on Cu-containing magnesium alloys and their related biological performance, the incorporation of copper into stainless steel, titanium alloys, and cobalt-based alloys has been observed to enhance the resistance against bacteria.[33–35] Additionally, Cu is a vital trace element that plays a pivotal role in the immune system,[36] the restoration of normal bone resorption rates,[37] and the enhancement of collagen fibre deposition.[38] For these reasons, it is an attractive candidate for use in concomitant bone regeneration and antibacterial applications. Liu *et al.* investigated a series of biodegradable Mg–Cu alloys, designed to induce osteogenesis, stimulate angiogenesis, and provide long-lasting antibacterial performance at the same time.[19] The immersion tests reported in Fig. 1 demonstrated that the corrosion resistance of the materials declined in direct proportion to the quantity of Cu present. This is due to the presence of an increased number of Mg_2Cu precipitates within the Mg matrix, which induces a more severe form of galvanic corrosion. In light of these considerations, we believe that the observed trend in the histomorphometric IDAr and dISAr parameters of the Solgel-Mg_SPF materials depended on a combination of two factors: primarily the implant site, and secondarily the presence of Cu during the early post-implantation phase. The above dual mechanism may also provide initial protection against infection, which is particularly beneficial in orthopaedic applications, creating a stable environment conducive to bone healing following surgical procedures.[19,39] However, due to possible cytotoxicity effects, the presence of Cu should be investigated. Thus, elemental analysis in the Solgel_Mg_SPF sample was performed.

2.5. SEM-EDS characterization

The Solgel_Mg_SPF sample alone was investigated by SEM-EDS. The analysis showed the absence of Cu in the degraded area of the implant, as seen in the representative image of Fig. 11. Representative SEM micrographs of the four different types of implants described in the study are reported (Fig. 12). The left column (images a–d) shows low-magnification views (500×), while the right column (images e–h) presents higher magnification images (2000×) of the regions highlighted by red rectangles in the corresponding left-column images. Images were acquired using backscattered electron detectors to enhance contrast and highlight compositional differences within the samples. In the micrographs, the light grey areas represent the implant material, which is surrounded by a darker grey region corresponding to the degraded implant. A dark grey zone, attributed to organic soft matter, is also visible. Newly formed bone appears in white, where trabecular bone structures can be distinguished.

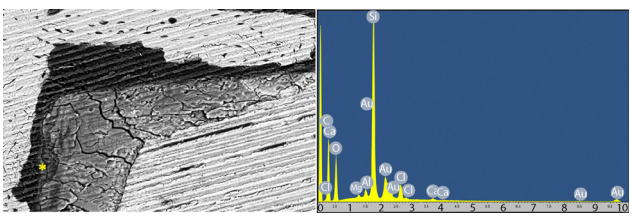

Fig. 11 (A) Representative SEM micrograph (Z contrast) and (B) X-ray spectrum acquired from a point at the interface of the sample Solgel_Mg_SPF. The spectrum is collected from the location marked by the yellow star.

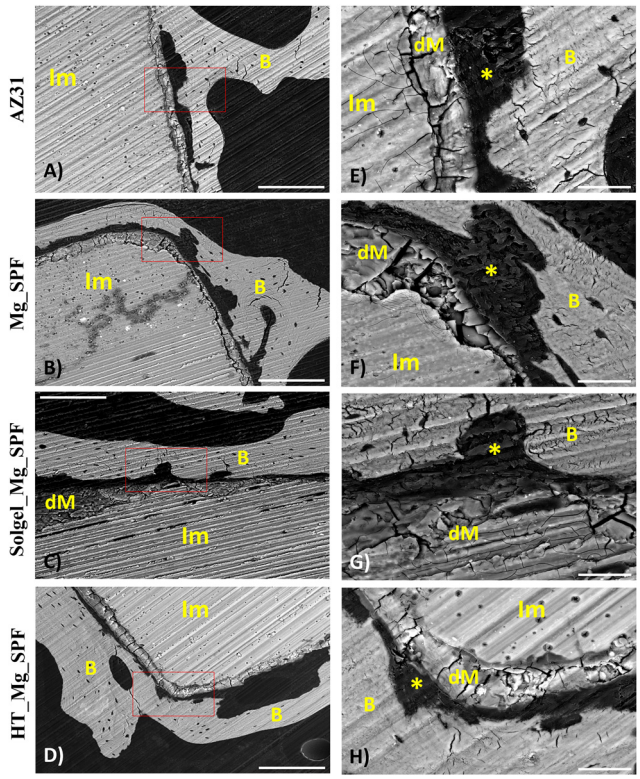

Fig. 12 Representative SEM micrographs of the four different types of implants described in the study. (A)–(D) Low-magnification views (500×) of the AZ31, Mg_SPF, Solgel_Mg_SPF, and HT_Mg_SPF samples respectively and (E)–(H) their zoomed-in images (2000×); in correspondence with the regions highlighted by red rectangles. Im = Impant; B = bone; dM = degraded material; * = organic soft matrix.

2.6. Atomic force microscopy nanoindentation

To test the mechanical response of the bone surface in correspondence to the various treatments, two regions of interest were first identified for each sample: the first (regenerated region, reg) corresponds to regenerated trabecular bone in the portion immediately close to the implant surface; in order to capture a possible influence of the treatment on the regenerative process, region reg was limited to a maximum distance of 50 μm from the implant, and the corresponding elastic modulus E_{reg} evaluated by nanoindentation onto 50 non-overlapping positions (Fig. 13). Then, averaged values obtained were compared with their counterparts (E_{nat}) obtained within region nat located at a macroscopic distance from the implant, where native trabecular tissue is present. The results in terms of relative percentage variation are shown in Table 1.

The measurement of the elastic modulus in zones regenerated (E_{reg}) and native (E_{nat}) using AFM nanoindentation yielded values in the about 1 to 2 GPa range, with detectable

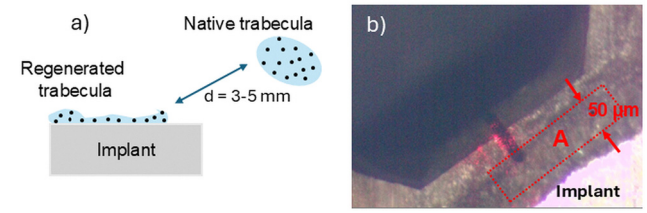

Fig. 13 AFM nanoindentation. (a) Selection of the region for AFM nanoindentation. (b) Detail of the cantilever-tip system when operating near to implant and specification of the regenerated region (reg).

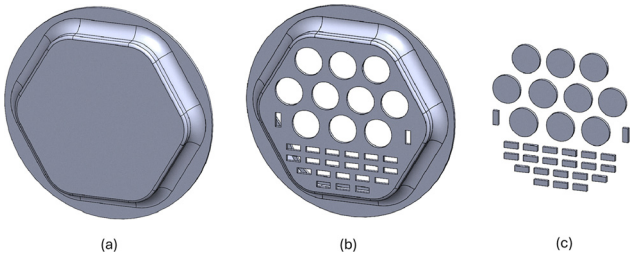

Fig. 14 Fabrication of material samples for the *in vivo* and *in vitro* tests. (a) 3D overview of the benchmark geometry manufactured *via* SPF process; (b) 3D overview of the formed blank after the samples' extraction *via* laser cutting for the subsequent *in vitro* (circles) and *in vivo* (rectangles) tests. (c) extracted samples for *in vitro* (circles) and *in vivo* (rectangles) tests.

fluctuations below 10% within each region, highlighting possible dependence on intrinsic characteristics of the sample such as its local morphology and composition; however, averaged values were consistent with previous results in the literature.[40] In this respect, it is noteworthy that all treatments, as evidenced in Table 1, resulted in a slight to robust increase of E in the regenerated tissue. In particular, in AZ31, this increase could be determined by a diffusion of Mg within the newly formed bone tissue, which causes the observed stiffness increase. This hypothesis appears to be supported by the fact that SPF or Solgel treatment could hinder the diffusion of the metal. In this sense, the relative increase observed in the HT_Mg_SPF implant may arise from a structural change due to the treatment and not be related to diffusion phenomena.

3. Experimental

3.1. Mg-device manufacturing by SPF process

A device having a benchmark geometry (Fig. 14) characterized by a hexagonal contour and a flat bottom was manufactured by SPF. The geometry of the part thus produced was chosen to highlight the capabilities of the process in creating components with a quite complex shape, but a flat bottom part was chosen to easily obtain the samples to be tested. As a starting blank, an AZ31 disk (D = 75 mm) 1 mm thick was used. The above-described component was created using a properly equipped OMCN P30/W 30 tons hydraulic press:[41] the AZ31 disk was clamped between two tools (the blankholder and the die), both surrounded by the coil of an induction heater, able to guarantee a uniform temperature (450 °C) in the forming chamber. Then, pressurized argon gas was inflated according to a profile calculated using finite element simulations, thus forcing the disk to copy the geometry of the die. After the manufacturing, 10 mm diameter circular and rectangular (5 mm × 2 mm) samples (Mg-SPF) were obtained from the flat part of the device by laser cutting for the subsequent *in vitro* and *in vivo* tests, respectively. A schematic representation of the component produced by SPF and of the extracted samples is shown in Fig. 14.

Table 1 Relative percentage variation of the elastic moduli from regenerated to native regions in correspondence with the different treatments

Sample	$(E_{reg} - E_{nat})/E_{nat}$
AZ31	+15.6%
Mg-SPF	+4.9%
Solgel_Mg_SPF	+9.0%
HT_Mg_SPF	+43.9%

After production, Mg-SPF samples were degreased by washing in acetone, acid pickled in a solution of 4 M acetic acid and 1 M nitric acid (Sigma-Aldrich, Merck) for 10 s to remove surface contaminants,[42] and then thoroughly rinsed in Milli-Q water for 5 min using an ultrasonic bath (Elmasonic S60, Elma Ultrasonic, DE). Sol–gel specimens doped with copper ions (Cu^{2+}) (Solgel_Mg_SPF) were obtained by dipping untreated Mg-SPF samples into a solution containing: the nanoparticles of $Mg(OH)_2$, the (3-glycidoxypropyl)-trimethoxysilane (GLYMO), and copper nitrate ($Cu(NO_3)_2$).[10] A 2.2 M NH_4OH solution was added drop by drop to a 0.4 M $MgCl_2$ solution to obtain $Mg(OH)_2$ nanoparticles. The silane solution was prepared by mixing GLYMO, 2-propanol, and distilled water with a volume ratio of 8 : 8 : 1. The $Cu(NO_3)_2$ was dissolved in the silane solution with a concentration of 0.04 M. Then, $Mg(OH)_2$ solution and GLYMO solution were mixed and kept under magnetic stirring for 2 h. Dip-coated samples were thermally treated in the oven at 160 °C for 2 hours to allow the densification and crystallization of the $Mg(OH)_2$-silane network. As for hydrothermal treatments (HT_Mg_SPF), they were performed by immersing the specimens in a Teflon-lined stainless steel hydrothermal synthesis reactor (Huanyu, Hangzhou Songhai Electronic Technology, CN) filled up to 70% with Milli-Q water. The reactor was then sealed and placed in a thermostatic oven at 160 °C for 4 : 30 hours (effective holding time of 4 hours). After a final ultrasound cleaning in Milli-Q water, the implants were individually placed in PA/PE double pouches, thermo-sealed, and then gamma-sterilized at 25.0 kGy.

3.2. Coatings characterization and SEM/EDS analysis

To investigate the general features of the applied solgel and hydrothermal coatings, the surface morphology of both sample groups (Solgel_Mg_SPF, and HT_Mg_SPF) was observed by scanning electron microscopy in secondary electrons (SE) mode using an EVO 50 SEM (Carl Zeiss, DE); such visual investigation allowed a first assessment of the coatings' quality and continuity. The crystalline phase composition of the coated samples was then assessed using an Empyrean X-ray diffractometer (Malvern Panalytical, UK), with excitation by a Cu Kα1 emitting

X-ray source operated at 40 kV voltage and 40 mA current intensity. The XRD spectra were collected in a 15°–70° 2θ range and phase matching was performed through the Panalytical Highscore Plus software. The SEM images reported in Fig. 12 were acquired using a Cambridge Stereoscan 200 electron microscope equipped with a Backscattered Electron (BSE) detector. Prior to imaging, a thin conductive layer of gold (thickness of ~4 nm) was applied to the surface of the samples *via* sputter-coating with an Edwards S150B apparatus. The microscope was operated at an accelerating voltage of 20 kV, with a beam current of 50 pA. The magnification range for the SEM images was set between 500× and 2000×. The detector's working distance was adjusted to 8.5 mm to optimize the imaging condition. Elemental analysis was performed using an energy dispersive X-ray spectroscopy (EDS) system integrated within the SEM microscope. The EDS spectra were acquired using the same parameters used for imaging, ensuring optimal excitation of the elements present in the sample. X-ray spectra were analyzed with Oxford INCA Energy 200 system. Lastly, electrochemical potentiodynamic polarization experiments were conducted to collect corrosion data of coated specimens through accelerated testing. Samples (n = 3) were masked with polyimide and insulation tape to leave an exposed area of 1 cm^2 and electrically connected as the working electrode to an Autolab PGSTAT30 potentiostat (Metrohm, NL), with a platinum counter electrode and an Ag/AgCl/saturated KCl reference electrode, both placed frontally to the exposed sample area at a 5 mm distance. Each test was carried out in 500 mL of fresh simulated body fluid (SBF, pH 7.4), prepared according to Kokubo's method,[43] at 37 ± 0.5 °C and in accordance with the ASTM G3 standard. During each test, the samples were left to corrode freely to let the system reach equilibrium at the material-specific open circuit potential (V_{OCP}) for 20 min. Next, the voltage applied to the system was varied around equilibrium, in a range between −0.5 V_{OCP} and +1.0 V_{OCP}, with a scan rate of 1 mV s^{-1}, and the corresponding current was measured at every point. A log(current)-voltage diagram was then generated for each test, and the free corrosion potential (E_{corr}) and corrosion current density (i_{corr}) values were extrapolated using the Tafel method[44] by the Metrohm NOVA software. Inductively coupled plasma optical emission spectroscopy (ICP-OES) was employed to determine the concentration of copper in the Solgel_Mg_SPF coatings, expressed as weight percentages (wt%). Samples were subjected to mineralization in an acidic medium, followed by appropriate dilution. Analyte calibration was performed using certified standard solutions. Each measurement was conducted in triplicate, and the reported values represent the mean. Analyses were carried out using a PerkinElmer Optima 8300 ICP-OES spectrometer.

3.3. Cytotoxicity

The cytotoxicity of Mg-based devices (Mg_SPF, Solgel_Mg_SPF, and HT_Mg_SPF) was evaluated in accordance with ISO 10993-12 and ISO 10993-5 guidelines. Briefly, murine fibroblast cells (L929) were cultured until reaching confluency. Post-confluency, the cells were treated with trypsin and seeded into 96-well plates at a density of 2.5 × 10^3 cells per 150 μL, then incubated at 37 °C with 5% CO_2. To prepare the conditioned media, samples were cleaned, sterilized, and incubated in DMEM complete medium for 72 hours, using a ratio of 0.2 g of Mg devices per 10 mL of DMEM. The supernatant was filtered using a 0.2 μm filter before initiating the cytotoxicity tests. After 24 hours, the culture media was replaced with 100 μL of the extract media. The same extract medium was maintained throughout the entire testing period without replacement, in order to evaluate the cumulative effects of degradation products. Positive and negative controls included 10% dimethyl sulfoxide (DMSO, 100 μL per well) and DMEM medium alone (100 μL per well), respectively. Cytotoxicity was assessed using the PrestoBlue® assay (Thermo Fisher) at intervals of 1, 3, and 7 days. A 1× PrestoBlue solution was added at 100 μL per well and incubated for 4 hours. Absorbance was measured at wavelengths of 570 nm and 600 nm using a Multiskan GO Microplate Spectrophotometer (Thermo Scientific). The Mg-based samples used for the indirect cytotoxicity assay were square-shaped with dimensions of 10 × 10 mm.

Cell viability and colonization patterns on Mg_SPF, Solgel_Mg_SPF, and HT_Mg_SPF were evaluated using fluorescent microscopy. Human dental pulp stem cells (DPSCs) were seeded at a density of 2 × 10^4 cells per implant surface and cultured in standard growth conditions (αMEM supplemented with 10% FBS, 37 °C, 5% CO_2) for periods of 1, 3, and 7 days. Cell viability was assessed using a dual-fluorescence assay combining Calcein-AM (live cell indicator) and Ethidium Homodimer-III (dead cell marker). Briefly, after the designated culture periods, samples were gently washed with PBS and incubated with the fluorescent probes for 30 min at 37 °C in the dark. Live cell distribution and morphology were visualized using confocal laser scanning microscopy (Leica SP8, Germany). Cell attachment patterns and spatial organization were analyzed across multiple fields of view. For standardization purposes, the magnesium specimens used in these assays were fabricated as square plates measuring 10 × 10 mm. Each experimental condition was tested in octuplicate (n = 8) and the experiment was independently repeated three times to ensure reproducibility. Human DPSCs were isolated from healthy donors following informed consent and in accordance with institutional ethical guidelines. Murine fibroblasts (L929 cell line) were obtained from the American Type Culture Collection (ATCC, Manassas, VA, USA).

3.4. Genotoxicity

The genotoxicity of Mg_SPF, Solgel_Mg_SPF, and HT_Mg_SPF was evaluated using the bacterial reverse mutation test following OECD guideline 471 for chemical testing [**https://www.oecd.org**] and with ISO 10993-12:2007 standards.

For this assay, samples were incubated in phosphate-buffered saline (PBS) at a ratio of 0.2 g mL^{-1} under conditions of 37 °C and 5% CO_2 for 72 hours. Before incubation, the samples were sterilized through one hour of UV irradiation, and the resulting extracts were utilized in the genotoxicity tests. Six different concentrations of Mg-SPF extracts (100%, 75%, 50%, 25%, 12.5%, and 6.25%) were tested for mutagenic

activity using two strains of *Salmonella Typhimurium* (TA1535 and TA1537). These strains were incubated overnight at 37 °C and 150 rpm, with and without the presence of the metabolic activation system provided by the microsomal fraction of rat liver (S9), employing the Ames MPF Penta 2 Format Mutagenicity Assay (Xenometrix AG, Allschwil, Switzerland). Positive control chemicals, including N4-aminocytidine (N4-ACT), and 9-aminoacridine (9-AAC) for S9-tests (without metabolic activation), and 2-aminoanthracene (2-AA) for S9+ tests (with metabolic activation), were supplied with the kit. The rat liver S9 fraction, along with the S9 100/1537 Booster solution, was also provided, specific to each strain for tests with and without metabolic activation (S9+/S9−), as per the supplier instructions. The growth medium served as the negative control. Briefly, 10 mL of growth medium was combined with 25 μL of the frozen stock culture of the tested strains (TA1535 and TA1537) and 10 μL ampicillin (Xenometrix). The cultures were incubated at 37 °C in a shaking incubator at 250 rpm for 14–16 hours. Culture density was assessed by measuring the optical density (OD) at 600 nm using a Microplate Spectrophotometer (Thermoscientific). Suitable OD values for testing were $\geq$2.0 for the cultures and $<$0.05 for the negative control. For the assays, 10 μL aliquots of extract derived from Mg alloy implants were added to S9−/S9+ plates with a final S9 fraction concentration of 4.5%. Following this, 240 μL of the suspension was transferred to 24-well plates, which were then sealed with breathable tape and incubated at 37 °C for 90 minutes with shaking at 250 rpm. After incubation, a reversion indicator medium (Xenometrix) was added to each well. The medium was gently mixed, and 50 μL per well was transferred to a 384-well microtiter plate. Each column of the 24-well plate was divided among 48 wells of the 384-well microtiter plate. Three plates were used per strain for both S9+/S9− conditions. The 384-well microtiter plates were placed in plastic bags to minimize evaporation and incubated at 37 °C for approximately 48 hours. The average number of revertant-containing wells per culture/dose was calculated. The criteria for scoring positive results included a fold increase (FI) over baseline $\geq$2 and a binomial *B*-value $\geq$0.99, determined using the software provided by Xenometrix (Calculation Workbook in MS Excel, created by M. Kamber, Xenometrix AG, 2012). Each extract concentration was tested in triplicate (n = 3) in three independent experiments for both S9+ and S9− conditions. We conducted the bacterial reverse mutation assay under two conditions: without metabolic activation to test the intrinsic mutagenicity of the parent compound, and with S9 mix to simulate liver metabolism and detect any mutagenic metabolites. This comprehensive strategy conforms to OECD 471 and ISO 10993 3 guidelines, covering both direct and metabolism-dependent genotoxic mechanisms and ensuring thorough evaluation.

3.5. *In vivo* experimental study

All animal procedures adhered to current Italian and European regulations concerning animal experimentation, specifically the European Directive 2010/63/EU and Italian Legislative Decree 26/2014. The experimental protocol and surgical procedures received approval from the Animal Welfare Body (OPBA) of the University of Palermo and were subsequently authorized by the Italian Ministry of Health (Authorization No. 434/2022-PR, dated July 19, 2022). This *in vivo* study was conducted and reported in compliance with the ARRIVE (Animal Research: Reporting of *in vivo* Experiments) guidelines to ensure transparency and reproducibility.[45] The sample size for the study was determined based on robust statistical considerations, ensuring compliance with the minimum requirements for histological analysis as specified by the UNI EN ISO 10993-6 standard, which mandates at least 10 implants per biomaterial evaluated. The calculation was performed using G*Power v.3.1.9.6 software (Franz Faul, University of Kiel, Germany), with the power level (1-β) set at 0.80 and the significance level α at 0.05. A power analysis employed a one-way ANOVA model, focusing on the type of biomaterial as a factor. Assuming an effect size $f > 0.45$ for the histomorphometric score concerning the percentage of bone-to-implant contact, it was established that a minimum of n = 48 implant sites are required, equating to n = 24 animals. Fig. 15 schematically illustrates the *in vivo* experimental study, from surgery to sample preparation and subsequent histological and nanomechanical analyses. Twenty-four male Sprague Dawley (SD) outbred rats, aged 8 weeks and weighing 225 ± 25 g, were sourced from Charles River Laboratories Italia S.r.l., Calco-LC, Italy, and housed in specific pathogen-free facilities equipped with surgical suites (ATeN Center of the University of Palermo, Palermo, Italy; Authorization No. 06/2017-UT dated March 30, 2017). The rats were kept in pairs within individually ventilated cages (Tecniplast SpA, Buguggiate/VA, Italy). The environmental conditions were maintained at a temperature of 23 ± 2 °C with a relative humidity of 55 ± 10%. Lighting was provided on a 12-hour light/dark cycle. Before surgery, the animals underwent a 10-day acclimatization period, with unrestricted access to pelleted maintenance feed (Standard diet 4RF18 Certificate - PF1611, Mucedola S.r.l., Settimo Milanese-MI, Italy) and water.

Surgeries were conducted under aseptic conditions and general anaesthesia, which was induced by intramuscular administration of 50 mg kg^{-1} ketamine (Lobotor 100 mg mL^{-1}, ACME Srl, Cavriago-RE, Italy) and 4 mg kg^{-1} xylazine (Rompun,

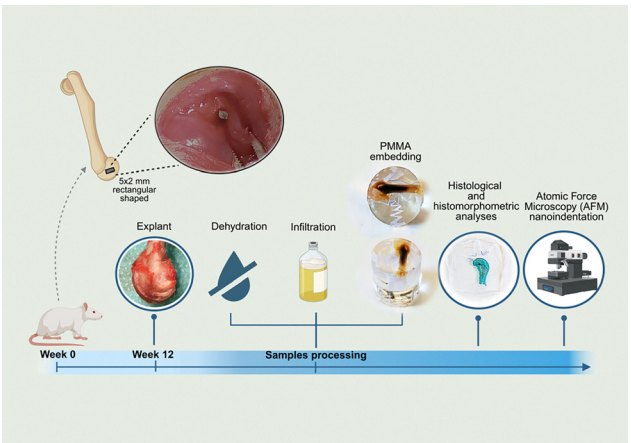

Fig. 15 Overview of the *in vivo* experimental workflow. PMMA = polymethylmethacrylate.

Bayer SpA, Milano, Italy). Anesthesia was sustained using 2% isoflurane in a 40%/60% air–oxygen mixture under spontaneous ventilation. Rats, weighing (415 ± 29) g, were positioned in a supine decubitus, and skin incisions were made on the lateral surface of both knees. After incising the joint capsule, the surface of the lateral femoral condyles of each knee was accessed. Bilateral cylindrical cortico-trabecular bone defects (approximately 2 mm in diameter and 6 mm in depth) were created using a sterile electric drill/mill (E-PEN DRIVE, Johnson & Johnson Medical S.p.A, Milan, Italy). Implants were press-fitted into the defects of each condyle in the following quantities, using a random combination of the types of biomaterials to be implanted: AZ31, serving as control (n = 12); Mg_SPF (n = 12); Solgel_Mg_SPF (n = 12); and HT_Mg_SPF (n = 12). Subsequently, the incisions were sutured layer by layer, and the rats were gradually brought out of anaesthesia. Each surgical procedure lasted approximately 30 minutes. Following implantation, the animals were closely monitored, with daily clinical evaluations conducted by the veterinary staff at the ATeN centre. Postoperative care included the administration of local anaesthetic ropivacaine, 0.01 mL (Ropivacaine Kabi 7.5 mg mL^{-1}—Fresenius Kabi Italia Srl, Isola della Scala VR, Italy) and a 1/3 controlled-release transdermal fentanyl patch applied at the base of the tail for 72 hours (MATRIFEN 25 μg $hour^{-1}$—Grunenthal Italia Srl, Milano, Italy). In addition, analgesic treatment (Meloxicam 2 mg kg^{-1}/die po, Metacam 0.5 mg mL^{-1} - Boehringer Ingelheim Italia, Milano, Italy) and antibiotic therapy (Enrofloxacin 5 mg kg^{-1}/die sc, Baytril 25 mg mL^{-1} - Bayer SpA, Milano, Italy) were provided for at least 5 days. Thereafter, the animals were checked weekly until the experimental endpoint at 90 days, at which time they were euthanized *via* intracardiac injection of 0.5 mL Tanax (Hoechst AG, Frankfurt-am-Main, Germany) following deep premedication with a combination of ketamine and xylazine, as previously described. Subsequently, the femurs were collected, meticulously cleared of adherent soft tissue, macroscopically assessed, and processed for further histological and mechanical evaluations.

3.6. Bone histology and histomorphometry

The explanted bone segments were initially fixed in 4% buffered paraformaldehyde, thoroughly washed under running water, and then dehydrated through a graded series of alcohol/water solutions for 24 hours each, beginning with 50% and 70% concentrations, followed by two passes in 95%. Complete dehydration was achieved through two passes in absolute alcohol, each lasting 24 hours. Next, the samples underwent infiltration with two different acrylate-based solutions (methacrylate from Merck KGaA, Darmstadt, Germany) for 24 hours each, before being embedded in a final polymethacrylate solution until full polymerization. Once polymerized, the bone segments were sectioned using a Leica 1600 diamond-bladed microtome (Leica SpA, Milano, Italy) to obtain sections 100–120 μm thick. These sections were further thinned to 40–60 μm with the Saphir polishing system (Saphir 550, ATM GmbH, Mammelzen, Germany). After polishing, the sections were stained histologically with Stevenel's Blue and counterstained with Fast Green. Digital images were then captured using a digital scanner (APERIO, Leica SpA, Milano, Italy).

The histomorphometric analysis was conducted using the high-throughput Bioquant Osteo histomorphometry system (Bioquant Image Analysis Corporation, Tennessee, USA), which employs standardized histomorphometry nomenclature.[46] For each implant, a rectangular region of interest (ROI) was defined, extending 0.5 mm diagonally from the implant corners (Fig. 16A). The bone histomorphometric parameters assessed included (Fig. 16A and B):

– Bone-to-implant contact (BIC, %): the percentage of direct contact between newly formed bone and the implant surface.

– Newly formed bone area (B.Ar/T.Ar, %): the percentage of newly formed bone within the surgical defect area.

– Trabecular thickness (Tb.Th, mm): the mean thickness of trabeculae, reflecting the trabecular structure.

– Trabecular separation (Tb.Sp, mm): the mean distance between adjacent trabeculae.

– Trabecular number (Tb.N, mm^{-1}): the number of trabeculae that a line through a trabecular compartment would hit per millimetre of its length (Fig. 16A and B).

Additionally, a square region of interest (ROI), measuring 1500 μm in both height and length, was evaluated to calculate the same histomorphometric parameters in native bone unaffected by the surgical intervention (Fig. 16C).

Finally, the implant-related histomorphometric parameters assessed included (Fig. 17):

– Degradation area (IDAr, %): determined by comparing the initial implant area and perimeter (outlined by the shadow remaining in the histological section) to those of the residual material.

– Variation of implant surface area (dISAr, %): calculated as the difference between the initial perimeter-to-area (BPm/BAr) ratio and that of the residual material, where higher values indicate increased surface irregularity and reduced compactness.

3.7. Atomic force microscopy nanoindentation

An atomic force microscope (NT-MDT, Moscow, Russia) was used as an indenter to collect the elastic (Young's) Modulus E of bone within the rectangular ROI, at distances <50 μm from the implant. AFM-based nanoindentation operates by a sharp tip (curvature radius $\approx$10 nm) placed on a side of an elastic cantilever with stiffness k = 25 N m^{-1}, which penetrates the surface

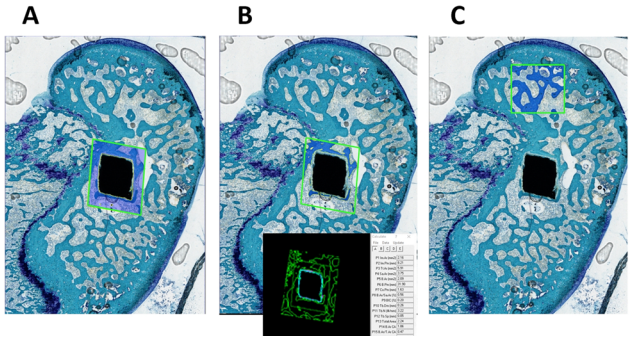

Fig. 16 Bioquant Image analysis. (A) ROI definition (blue rectangle); (B) histomorphometric parameters evaluated in the defined ROI; (C) ROI definition (blue square) measuring 1500 μm in height and 1500 μm in length utilized for the assessment of the histomorphometric parameters of the native bone.

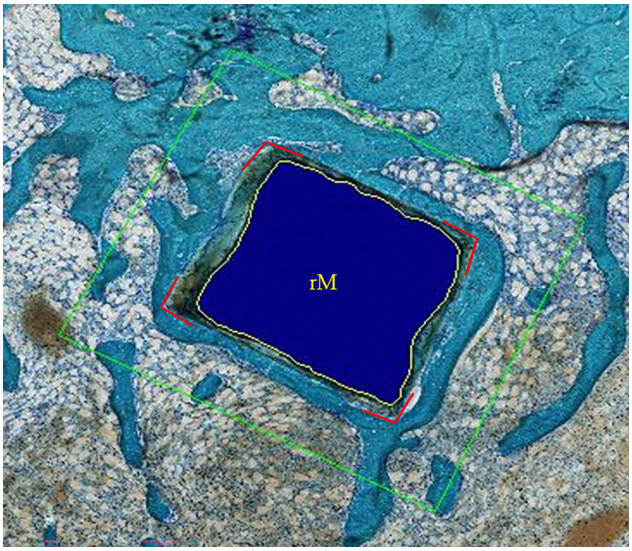

Fig. 17 Representative image for the determination of the IDAr and dISAr parameters. The red lines indicate the angles of the shadow left by the initial material as it degraded; rM = residual material.

of a nanometric amount (20 ± 5) nm. The penetration causes mechanical deflection of the elastic cantilever. Such deflection is measured and transformed into a Force-penetration depth curve by an opportune calibration operation. The Young's modulus (Y) of the surface at the point of nanoindentation is then extracted by an opportune fitting model for the experimental curve. In this work, 50 curves were acquired onto as many non-overlapped positions of the surface; therefore, Y values extracted from each curve were obtained as an average. The Y values were obtained by fitting the experimental curves by a Hertzian model already used for evaluations of bone.[47] The nanoindentation zone is established with micrometric accuracy combining histological and optical images. This prevents possible biases such as PMMA deposits, bone lacks, *etc.*

3.8. Statistical analysis

Statistical analysis was conducted utilizing GraphPad Prism Suite (v.8.0.2, GraphPad Software, La Jolla, CA). Data are reported as Mean ± SD, and statistical significance thresholds were fixed at $p < 0.05$. Statistical evaluation of mutagenicity *via* the Ames test incorporated two stringent acceptance criteria: (i) a fold increase (FI) ≥2.0 over the baseline and (ii) a binomial B-value threshold of ≥0.99. For each concentration, six replicate wells containing revertants were analyzed, with quantitative assessment performed using a standardized Excel-based computational template (Kamber, Xenometrix AG, 2012). Histomorphometric results were analyzed with a one-way ANOVA test by considering implant type as a fixed factor, followed by *post hoc* multiple comparisons of Mg_SPF, Solgel_Mg_SPF, and HT_Mg_SPF *versus* AZ31 using Dunnett's test.

4. Conclusions

In summary, the comprehensive characterization of novel Mg alloy implants provides significant insights into their potential as biodegradable medical devices. *In vitro* analyses demonstrated exceptional biocompatibility for both hydrothermal and sol–gel-modified surfaces, exhibiting sustained cell viability and no genotoxic effects. *In vivo* investigations revealed complex tissue-material interactions, with all implant variants supporting *peri*-implant bone formation, although surface-treated implants exhibited reduced BIC compared to the control. Notably, despite the uniformity and seamlessness of the applied coating, the Solgel_Mg_SPF implants showed accelerated degradation kinetics, primarily attributed to the combination of copper ion incorporation in the surface coating and the implants' placement in highly vascularized areas, both of which contribute to a higher degradation rate. Although modified surfaces exhibited lower bone-implant contact percentages compared to controls, and the formation of an intermediary calcification matrix suggests an alternative integration pathway warranting further investigation. Notably, both the improvement of the elastic modulus of the regenerated tissue in HT_Mg_SPF implants and the observed hydrogen gas evolution, particularly in Solgel_Mg_SPF implants, require consideration for clinical application. While not hindering overall tissue integration, these results underscore the need to optimize degradation rates for specific applications, as well as to further refine the translation of *in vitro* corrosion data towards *in vivo* scenarios. The differential response to surface treatments offers valuable insights for tailoring implant properties to specific medical uses. It should be noted that the present study is not without limitations. Firstly, the lack of a different experimental time point precludes an assessment of the bone response to the implants in terms of bone maturation and osseointegration, as well as the degradation rate of the implant over time. Secondly, further investigations, including osteogenic gene response, microtomographic analysis, and other histological staining specific to the mineralization process, such as Alizarin Red, could be useful for comparing our histological, histomorphometric, and AFM results. Such a comparison would have been beneficial to ascertain the degree of mineralization of the *peri*-implant bone.

These findings enhance our understanding of Mg-based implant behavior in biological systems, establishing a foundation for next-generation biodegradable implants. Future research should focus on long-term studies to characterize bone maturation processes and refine surface modifications to optimize degradation kinetics. The promising results encourage continued development while highlighting areas for improvement to enhance therapeutic potential.

Author contributions

Daniele Bellavia: conceptualization: equal; methodology: lead; supervision: equal; writing – original draft: lead; writing – review & editing: equal. Francesco Paduano: conceptualization: lead; formal analysis: equal; methodology: lead; supervision: equal; validation: lead; writing – original draft: lead; writing –review & editing: equal. Silvia Brogini: data curation: lead; investigation: lead; methodology: equal; visualization: lead; writing – original draft: equal;

writing – review & editing: lead. Roberta Ruggiero: data curation: supporting; formal analysis: supporting; investigation: supporting; methodology: supporting; writing – original draft: supporting. Rosa Maria Marano: data curation: supporting; formal analysis: supporting; investigation: supporting; methodology: supporting. Angela Cusanno: conceptualization: equal; formal analysis: equal; methodology: equal; validation: equal; writing – original draft: equal. Pasquale Guglielmi: conceptualization: equal; formal analysis: equal; methodology: equal; validation: equal; writing – original draft: equal. Antonio Piccininni: conceptualization: equal; formal analysis: equal; methodology: equal; validation: equal; writing – original draft: equal. Matteo Pavarini: investigation: equal; methodology: equal. Agnese D'Agostino investigation: equal; methodology: equal. Alessandro Gambardella: investigation: supporting; visualization: supporting; writing– original draft: supporting; writing – review & editing: supporting. Gianfranco Palumbo: conceptualization: equal; formal analysis: equal; funding acquisition: lead; methodology: equal; validation: equal; writing – original draft: equal. Roberto Chiesa: funding acquisition: lead; methodology: equal; project administration: lead; resources: lead; supervision: equal. Gianluca Zappini: resources: equal. Marco Tatullo: funding acquisition: lead; investigation: lead; project administration: lead; resources: lead; supervision: supporting; writing – review & editing: supporting. Gianluca Giavaresi: conceptualization: lead; formal analysis: equal; funding acquisition: lead; project administration: lead; resources: lead; validation: lead.

Conflicts of interest

There are no conflicts to declare.

Data availability

The datasets generated and analyzed during the current study are available in the Figshare repository at the following DOI: **https://doi.org/10.6084/m9.figshare.29166155**. All raw and processed data supporting the findings are openly accessible.

Supplementary information is available. See DOI: **https://doi.org/10.1039/d5tb01282a**

Acknowledgements

This research was funded by the CONTACT project (Grant: ARS01_01205, PON R&I Funds 2014-2020 and FSC, Ministry of University and Research) ''CustOm-made aNTibacterial/bioActive/bioCoated prosTheses.'' The Marrelli Health project is registered under CUP code number B19J20000490005. The authors would like to thank Professor Maria Grazia Zizzo and Dr Fabrizio Di Pietra for their active collaboration in the *in vivo* study.

References

1 G. Giavaresi, D. Bellavia, A. De Luca, V. Costa, L. Raimondi, A. Cordaro, M. Sartori, S. Terrando, A. Toscano, G. Pignatti and M. Fini, *Int. J. Mol. Sci.*, 2023, **25**, 282.
2 I. Antoniac, M. Miculescu, V. Mănescu (Păltânea), A. Stere, P. H. Quan, G. Păltânea, A. Robu and K. Earar, *Materials*, 2022, **15**, 1148.
3 M. P. Staiger, A. M. Pietak, J. Huadmai and G. Dias, *Biomaterials*, 2006, **27**, 1728–1734.
4 S. Seetharaman, D. Sankaranarayanan and M. Gupta, *J. Funct. Biomater.*, 2023, **14**, 324.
5 D. Krüger, S. Galli, B. Zeller-Plumhoff, D. C. F. Wieland, N. Peruzzi, B. Wiese, P. Heuser, J. Moosmann, A. Wennerberg and R. Willumeit-Römer, *Bioact. Mater.*, 2022, **13**, 37–52.
6 D. Sorgente, G. Palumbo, A. Piccininni, P. Guglielmi and S. A. Aksenov, *CIRP J. Manuf. Sci. Technol.*, 2018, **20**, 29–35.
7 G. Palumbo, G. Ambrogio, A. Crovace, A. Piccininni, A. Cusanno, P. Guglielmi, L. De Napoli and G. Serratore, *Metals*, 2022, **12**, 293.
8 Z. Savaedi, R. Motallebi, H. Mirzadeh, R. Mehdinavaz Aghdam and R. Mahmudi, *Curr. Opin. Solid State Mater. Sci.*, 2023, **27**, 101058.
9 S. Brogini, A. Crovace, A. Piccininni, G. Serratore, G. Marchiori, M. Maglio, P. Guglielmi, A. Cusanno, L. De Napoli, R. Conte, M. Fini, G. Ambrogio, G. Palumbo and G. Giavaresi, *Sci. Rep.*, 2024, **14**, 7959.
10 M. Tatullo, A. Piattelli, R. Ruggiero, R. M. Marano, F. Iaculli, C. Rengo, I. Papallo, G. Palumbo, R. Chiesa, F. Paduano and G. Spagnuolo, *Dent. Mater.*, 2024, **40**, 557–562.
11 V. Costa, L. Raimondi, S. D. Scilabra, M. L. Pinto, D. Bellavia, A. De Luca, P. Guglielmi, A. Cusanno, L. Cattini, L. Pulsatelli, M. Pavarini, R. Chiesa and G. Giavaresi, *Materials*, 2025, **18**, 1254.
12 F. Witte, N. Hort, C. Vogt, S. Cohen, K. U. Kainer, R. Willumeit and F. Feyerabend, *Curr. Opin. Solid State Mater. Sci.*, 2008, **12**, 63–72.
13 A. C. Hänzi, I. Gerber, M. Schinhammer, J. F. Löffler and P. J. Uggowitzer, *Acta Biomater.*, 2010, **6**, 1824–1833.
14 J.-L. Wang, J.-K. Xu, C. Hopkins, D. H.-K. Chow and L. Qin, *Adv. Sci.*, 2020, **7**, 1902443.
15 X. Guo, Y. Hu, K. Yuan and Y. Qiao, *Materials*, 2022, **15**, 3291.
16 A. Miklaszewski, K. Kowalski and M. Jurczyk, *Metals*, 2018, **8**, 894.
17 F. Romero-Gavilán, I. García-Arnáez, A. Cerqueira, L. Scalschi, B. Vicedo, A. Villagrasa, R. Izquierdo, M. Azkargorta, F. Elortza, M. Gurruchaga, I. Goñi and J. Suay, *Biomater. Sci.*, 2023, **11**, 1042–1055.
18 A. Jacobs, G. Renaudin, C. Forestier, J.-M. Nedelec and S. Descamps, *Acta Biomater.*, 2020, **117**, 21–39.
19 C. Liu, X. Fu, H. Pan, P. Wan, L. Wang, L. Tan, K. Wang, Y. Zhao, K. Yang and P. K. Chu, *Sci. Rep.*, 2016, **6**, 27374.
20 Y. Castro Martín and A. Durán, *J. Sol-Gel Sci. Technol.*, 2019, **90**, 198–208.
21 J. P. Fernández-Hernán, B. Torres, A. J. López and J. Rams, *Gels*, 2022, **8**, 426.
22 J. Wang, S. Deng, M. Meng, W. Tu and J. Ou, *Surf. Coat. Technol.*, 2023, **454**, 129157.
23 R. Ruggiero, R. Marano, A. Facente, E. Aiello, R. Conte, G. Serratore, G. Ambrogio, F. Paduano and M. Tatullo, *Soc. Sci. Res. Netw.*, 2024, 4957726, DOI: **10.2139/ssrn.4957726**.

24 J. Kubásek, D. Vojtěch, E. Jablonská, I. Pospíšilová, J. Lipov and T. Ruml, *Mater. Sci. Eng. C*, 2016, **58**, 24–35.
25 J.-W. Lee, H.-S. Han, K.-J. Han, J. Park, H. Jeon, M.-R. Ok, H.-K. Seok, J.-P. Ahn, K. E. Lee, D.-H. Lee, S.-J. Yang, S.-Y. Cho, P.-R. Cha, H. Kwon, T.-H. Nam, J. H. L. Han, H.-J. Rho, K.-S. Lee, Y.-C. Kim and D. Mantovani, *Proc. Natl. Acad. Sci. U. S. A.*, 2016, **113**, 716–721.
26 D. Noviana, D. Paramitha, M. F. Ulum and H. Hermawan, *J. Orthop. Translat.*, 2015, **5**, 9–15.
27 L. Chang, Y. Luo, W. Li, F. Liu, J. Guo, B. Dai, W. Tong, L. Qin, J. Wang and J. Xu, *Regener. Biomater.*, 2024, **11**, rbae095.
28 N. Kawamura, Y. Nakao, R. Ishikawa, D. Tsuchida and M. Iijima, *Materials*, 2020, **13**, 473.
29 T. Kraus, S. F. Fischerauer, A. C. Hänzi, P. J. Uggowitzer, J. F. Löffler and A. M. Weinberg, *Acta Biomater.*, 2012, **8**, 1230–1238.
30 M. H. Larsen, J. C. Walmsley, O. Lunder, R. H. Mathiesen and K. Nisancioglu, *J. Electrochem. Soc.*, 2008, **155**, C550.
31 H. Zhan, J. M. C. Mol, F. Hannour, L. Zhuang, H. Terryn and J. H. W. de Wit, *Mater. Corros.*, 2008, **59**, 670–675.
32 W. J. Liang, P. A. Rometsch, L. F. Cao and N. Birbilis, *Corros. Sci.*, 2013, **76**, 119–128.
33 H. Chai, L. Guo, X. Wang, Y. Fu, J. Guan, L. Tan, L. Ren and K. Yang, *J. Mater. Sci.: Mater. Med.*, 2011, **22**, 2525–2535.
34 S. Wang, C. Yang, L. Ren, M. Shen and K. Yang, *Mater. Lett.*, 2014, **129**, 88–90.
35 R. Liu, Y. Tang, L. Zeng, Y. Zhao, Z. Ma, Z. Sun, L. Xiang, L. Ren and K. Yang, *Dent. Mater.*, 2018, **34**, 1112–1126.
36 L. Lan, Z. Feng, X. Liu and B. Zhang, *J. Cell. Mol. Med.*, 2024, **28**, e18390.
37 T. Wilson, J. M. Katz and D. H. Gray, *Calcif. Tissue Int.*, 1981, **33**, 35–39.
38 C. Gérard, L.-J. Bordeleau, J. Barralet and C. J. Doillon, *Biomaterials*, 2010, **31**, 824–831.
39 M. Qiao, J. Sha, S. Yin, W. Liu, Z. Zhao, J. Cui and Z. Zhang, *J. Mater. Res. Technol.*, 2022, **18**, 1607–1622.
40 M. Asgari, J. Abi-Rafeh, G. N. Hendy and D. Pasini, *J. Mech. Behav. Biomed. Mater.*, 2019, **93**, 81–92.
41 A. Cusanno, P. Guglielmi, D. Sorgente and G. Palumbo, *Adv. Manuf.*, 2025, **13**, 284–302.
42 B. R. Fazal and S. Moon, *J. Korean Inst. Surf. Eng.*, 2016, **49**, 231–237.
43 T. Kokubo and H. Takadama, *Biomaterials*, 2006, **27**, 2907–2915.
44 A. Atrens, G.-L. Song, Z. Shi, A. Soltan, S. Johnston and M. S. Dargusch, *Encyclopedia of Interfacial Chemistry*, ed K. Wandelt, Elsevier, Oxford, 2018, pp. 515–534.
45 C. Kilkenny, W. J. Browne, I. C. Cuthill, M. Emerson and D. G. Altman, *PLoS Biol.*, 2010, **8**, e1000412.
46 A. M. Parfitt, M. K. Drezner, F. H. Glorieux, J. A. Kanis, H. Malluche, P. J. Meunier, S. M. Ott and R. R. Recker, *J. Bone Miner. Res.*, 1987, **2**, 595–610.
47 M. Bontempi, F. Salamanna, R. Capozza, A. Visani, M. Fini and A. Gambardella, *Materials*, 2022, **15**, 7512.

